Turbulence model assessment for the characterization of highly-loaded compressor stages

Riccardo Toracchio

Turbomachinery and Propulsion Department, von Karman Institute for Fluid Dynamics, Belgium, riccardo.toracchio@vki.ac.be

Supervisor: Fabrizio Fontaneto

Associate Professor, Turbomachinery and Propulsion Department, von Karman Institute for Fluid Dynamics, Belgium, fabrizio.fontaneto@vki.ac.be

University Supervisor: Koen Hillewaert

Associate Professor, Aerospace and Mechanical Engineering Department, University of Liège, Belgium, koen.hillewaert@uliege.be

Abstract

The turbulence model still represents a weak point of RANS simulations when dealing with complex turbomachinery flows. This is true especially for models based on the Boussinesq's isotropic eddy viscosity assumption that provide poor performance in a large variety of flow conditions, such as strong adverse pressure gradients and recirculating regions. In presence of large blade loadings the turbulence model can impact severely on the prediction of the low-momentum flow at the end-walls and influence the entire structure of secondary flows in the blade passage, with an important effect on the computed global performance. This paper presents a turbulence model comparison for the characterization of a highly-loaded low-pressure compressor at multiple operating points using 3D RANS simulations. The turbulence models employed are: Spalart-Allamars, Chien k-epsilon and Menter k-omega SST, which are frequently used for the design of axial compressors. The aim is to provide an overview of the implications of using a specific turbulence model, with a clear physical description of their impact on the critical flow features of the machine. Comparisons against experimental results are then used to assess the reliability of the models at design and near-stall conditions. It will be shown that for this type of compressors no single turbulence model is generally better than others and the prediction depends on the operating point analysed, with discrepancies increasing at reduced mass-flow operating conditions.

Keywords: Compressor, turbulence, CFD, secondary flows

1. Introduction

Several studies have been carried out in the past with the aim to characterize three-dimensional separations and secondary flows [1; 2; 3], which are considered the main source of losses in axial compressors, with relevant impact especially when approaching the stability of the machine. The role of the CFD in predicting the impact of these mechanisms has been increasingly important in the last years, up to the point that it is nowadays considered essential during the design process of turbomachinery [4; 5]. At the present state, RANS techniques are the most feasible solution to investigate turbomachinery flows and for compressor design, given still the large limitations of more time consuming approaches (such as LES and DNS) [6; 7]. However, the weakest point of RANS simulations is that the turbulence model adopted impacts severely on the prediction of the secondary flow structures. Turbulence model assessment on transonic axial compressors was performed in [8; 9; 10; 11; 12; 13]. The authors found that limited to the presented application, the SST model provided better performance in separated flow regions, followed by $k-\epsilon$ and Spalart-Allmaras (SA) turbulence models. However, no turbulence model is generally better than others in predicting real and complex flow features [14], especially in compressors develop-

ing large scale structures. The effect of the turbulence model on an axial compressor known to develop large scale vortices, such as tip-leakage and corner vortices, was analyzed in [15]. In the tip region the best prediction was provided by the SST model, while close to the hub it was the $k-$ to have superior performance against experimental results. Linear compressor cascades with highly-loaded blades were analysed in [16; 17; 18]. The $k-\epsilon$ model showed more reliable results, with respect to the SST and Spalart Allmaras, for what concerns the size and the intensity of the hub corner separation. However, these studies highlighted that the performance of the turbulence models is case-by-case dependent, and no general conclusion can be drawn about their reliability and accuracy.

The objective of this paper is to provide a turbulence model assessment for an highly-loaded low-pressure compressor by means of 3D RANS simulations. The models mostly used for the design of turbomachinery are considered: Menter $k-\omega$ SST and Chien $k-\epsilon$ turbulence models. Also results for the Spalart Allmaras model will be briefly described despite no results were available at near-stall conditions. The DREAM compressor, installed in the VKI R4 facility, and representative of the first stage of a modern low pressure compressor, will be used for this purpose. The main idea is to provide a physical explanation to the evolution of secondary flow structures appearing at operating points with reduced mass-flow, while highlighting advantages and drawbacks of the employed turbulence models by means of the validation against the experimental results.

2. Compressor test-rig and instrumentation

2.1. Experimental facility and test section

The VKI R4 facility is a closed-loop high-speed test-rig, composed by a tank used as settling chamber (1), the test section (2), a discharging collector at the compressor outlet (3), a return channel to guide the air back to the reservoir (4), and a throttling valve to run the compressor at different operating conditions (5) (Figure 1). An independent variation of temperature and pressure into the facility is possible by means of the heat exchanger (located upstream of the test compressor) and the closed-loop configuration, allowing to test cruise and take-off aircraft conditions. The test section considered is the DREAM compressor stage: a 1.5 stage, with equal number of inlet guide vanes (IGV) and outlet guide vane (OGV) stators, representative of the first stage of a low-pressure compressor (Figure 2, where the measurement planes are clearly identified).

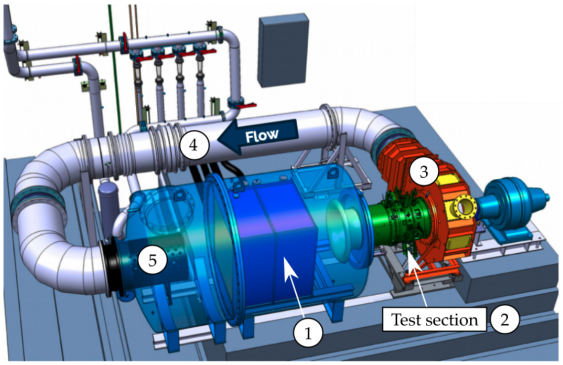

Figure 1: von Karman Institute R4 facility: closed-loop high-speed compressor test rig.

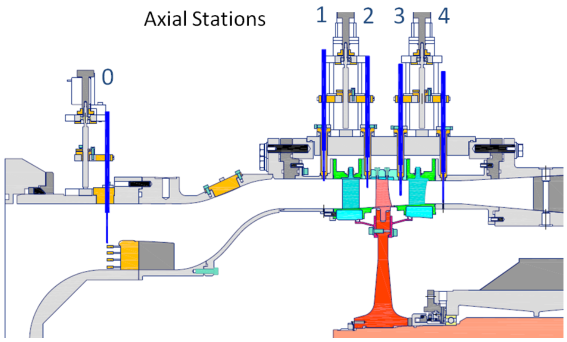

Figure 2: Dream test section.

2.2. Test section instrumentation

Probe traversing is allowed at four circumferential locations (0°, 90°, 180° and 270°) and for each measurement plane, axially located at stage inlet (plane 1), IGV outlet (plane 2), rotor outlet (plane 3) and stage outlet (plane 4). In this way, good resolution measurements of total pressure, temperature, Mach number and flow angles can be performed to properly characterize each location of the machine. For the measurement of the global performance, 4 combined total pressure and total temperature rakes are distributed circumferentially in plane 0, located upstream of plane 1, and in plane 4. A constant rotational speed of the compressor and a variation of the throttling valve position allow to retrieve the compressor map. +/- 0.00053 and 0.7% of the mass-flow at design conditions are the uncertainty respectively associated to the pressure ratio and the mass-flow.

A fast-response pressure probe, employed to obtain the phase-locked-average total pressure maps, is located at the rotor outlet and employed with acquisition frequency of 10Mhz for 10 seconds. It is characterized by resonance frequency of around 300 kHz and uncertainty calibration of +/- 1.8 mbar.

These uncertainty values are presented in a 95% confidence interval and calculated with the ASME method [19]. Further information about the test section instrumentation can be found in [20].

3. Numerical approach

3.1. Numerical setup

Fully-turbulent compressible RANS equations were solved by means of Numeca Fine/Turbo, and spatially discretized with a cell-centered finite volume formulation on a multi-block structured grid. At the inlet the total pressure and temperature retrieved with experiments were imposed, together with the turbulence intensity and viscosity ratio. The mass-flow boundary condition was imposed at the outlet. Air was considered as a calorically perfect gas, and the solid walls as adiabatic. An explicit multi-stage Runge-Kutta method combined with an implicit residual smoothing approach was considered for the time integration to a steady-state condition. Non reflecting boundary conditions with mixing plane approach were employed at the rotor-stator interfaces. For the turbulent closure, the Menter $k-\omega\ SST$, Chien $k-\epsilon$ and Spalart-Allmaras turbulence models were considered. Due to the divergence of the solution at near-stall (NS) conditions, the results for the SA model are only available at design (DE) and middle (MID) operating points. The formulation of the aforementioned models can be found in [21].

3.2. Numerical domain and mesh

3.2.1. Numerical domain

The role of real geometrical features, such as fillets and cavities, was assessed to understand their impact on the global performance and flow field of the machine. Fillets have been integrated into the domain due to their influence on the secondary flows structures and limited impact on mesh size, while the cavities have not been taken into account. Indeed, given their closed geometry on the test facility, they have very limited impact at rotor and stator inlets. Moreover, the rotor tip gap was set to the averaged measured value and hot geometries (i.e. in rotation) were employed. A meridional section and a blade-to-blade cut at 50% of the span of the presented compressor are reported respectively in Figure 3a and 3b.

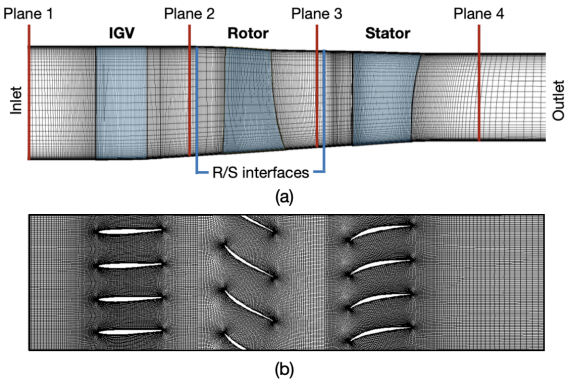

Figure 3: Numerical domain: meridional view (a) and B2B cut 50% span with channel repetition (b) on a coarser mesh.

In the present paper only the 100% speed of the compressor will be investigated.

3.2.2. Mesh quality

Autogrid5 and IGG softwares were used to generate a multi-block structured mesh. An O4H symmetric B2B topology and a OH topology ware considered for every blade row and the rotor tip gap region. For the creation of the hub and shroud fillets a B2B section offset method was considered, with 35 span-wise points and a minimum angle of 25° to guarantee a good distribution and angular deviation of the wall points. 81 cells and 20% constant size cells in the mid-flow gap region were used in the span-wise direction, and skewness level, maximum aspect and expansion ratios were set to provide good quality results. A value of y+ lower than 1.2 was guaranteed everywhere, while expansion ratio and cell width were adjusted to ensure a uniform distribution of cells at the wall.

Global performance and percentage difference of total pressure at the rotor outlet are reported in Figure 4 and Figure 5 considering a coarse, medium and fine mesh solution with 1.2, 9.2 and 73.8 million cells respectively. The fine mesh is here considered as reference case. An isotropic refinement by a factor of 2 was performed in the θ, R and Z directions. The rotor outlet region is considered as the most critical for the phenomena described in the present paper, and for this reason is chosen as location for the comparison. This study was performed with the $k-\omega\ SST$ turbulence model at DE conditions.

The good accuracy level of the medium mesh with respect to the reference, and the reduced computa-

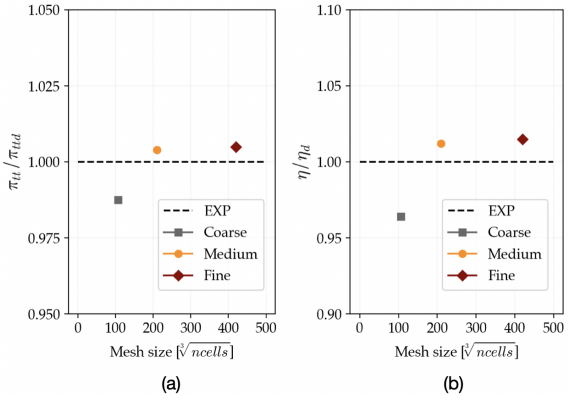

Figure 4: Comparison among mesh levels on the pressure ratio (a) and efficiency (b) of the compressor.

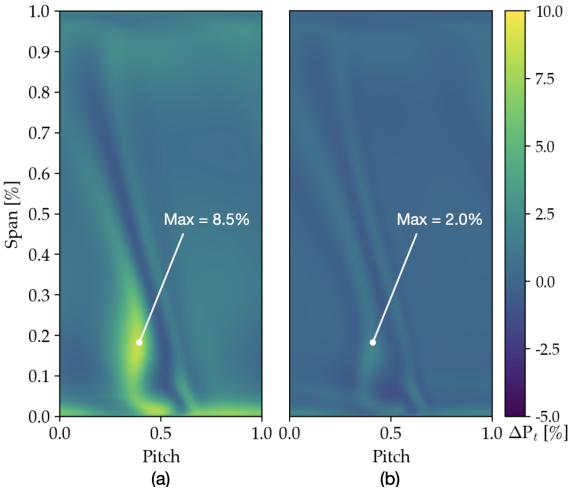

Figure 5: Percentage difference of the coarse mesh (a) and medium mesh (b) with respect to the reference case on the rotor outlet total pressure map.

tional cost, made it suitable to be employed in the simulations. The coarse solution, instead, as shown in Figure 5, presents discrepancies up to 8.5% when compared to the reference case due to the numerical dissipation induced in the recirculating regions of the flow, over-predicting the total pressure reduction.

4. Results

4.1. Overall observations

The large loading of the rotor blade and the high degree of reaction make the rotor a possible region for the development of critical secondary flow structures. In particular, the tested compressor presents a large value of the loading in the hub region, supporting the need of further investigating the development of the flow in this region. Figure 6 shows the skin friction lines on the rotor hub wall.

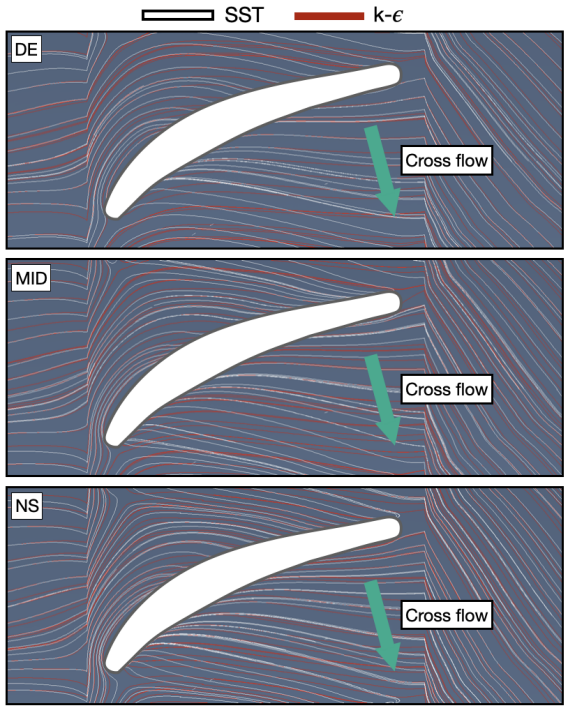

Figure 6: Skin friction lines on the rotor hub wall for SST (white line) and $k-\epsilon$ (red line) models.

From this picture, it is evident that a strong difference is present between the two turbulence models which highly impacts on the flow pattern in the rotor hub region. The SST turbulence model presents, indeed, larger cross-flow in the channel with respect to the $k-\epsilon$, pushing low-momentum flow on the suction side of the adjacent blade and possibly allowing the development of a more critical flow structure in that region. This is further enhanced by the impact of the horseshoe vortex legs in the rear part of the blade, contrarily to the $k-\epsilon$ turbulence model.

Given this evidence, the origin of such behavior and the large-scale effects induced in the entire machine need to be analysed and assessed. The intent is to quantify the differences between the investigated turbulence models and identify the physical quantities driving these secondary mechanisms since their earliest appearance. To do so, the flow quantities at rotor inlet will be firstly observed to understand the influence of inlet conditions on the evolution of the flow field, and then analysing the impact that such flow conditions may have downstream of the rotor blade.

4.2. *Flow conditions at the rotor inlet*

Figure 7a presents the bottom 50% span of the relative flow angle for DE, MID and NS conditions. At reduced mass-flow, discrepancies in the value of the incidence start to appear, and this become visible at MID condition for span lower than 25%. This is even more evident at near-stall condition, where a blockage effect appears in the blade passage that not only impacts the incidence, but also the axial velocity (Figure 7b). This may demonstrate the appearance of a large secondary structure which impacts on the blockage of the passage at NS conditions for the SST turbulence model. However, the skin friction lines around the LE do not reveal any relevant difference as the stagnation point is the same for both models.

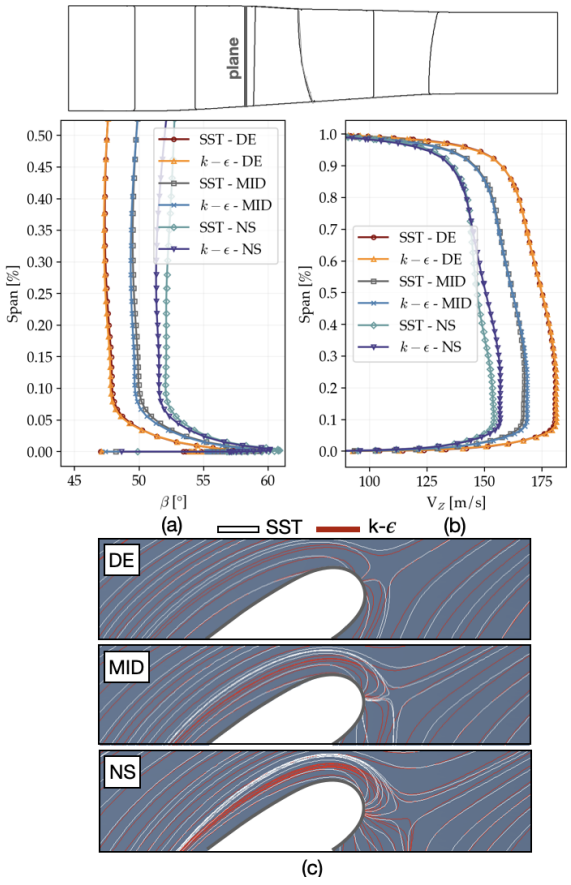

Figure 7: Rotor inlet conditions: relative flow angle (a), axial velocity (b) and hub-wall skin friction lines around the LE (c), at DE, MID AND NS conditions for SST and $k-\epsilon$ turbulence models.

Figure 8 presents the span-wise pitch-averaged distribution of the turbulent viscosity at the inlet and outlet of the rotor, non-dimensionalized with the dynamic viscosity of the flow.

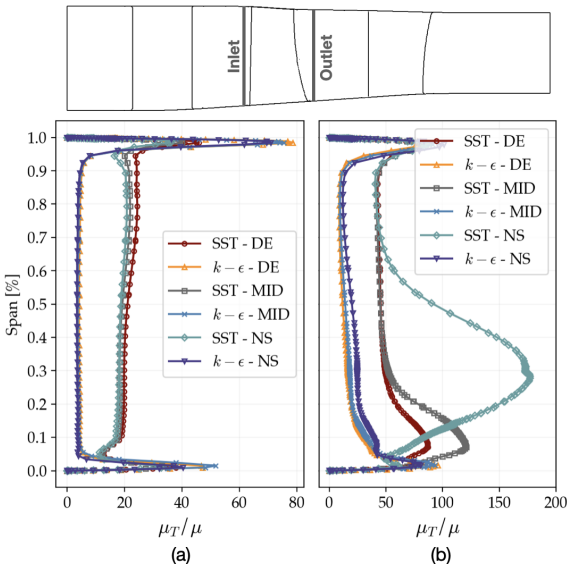

Figure 8: Span-wise distribution of eddy viscosity at rotor inlet (a) and outlet (b).

From the picture two opposite trends appear outside and inside the BL at the rotor inlet. Outside of the boundary-layer, the SST turbulence model presents indeed a larger value of the turbulent viscosity, while into the boundary-layer the trend is inverted. At rotor outlet, an overall increase of the eddy viscosity is visible due to the turbulent action determined by the development of a possible hub corner separation, as expected from a highly-loaded rotor in the hub region. However, the increase of the eddy viscosity from inlet to outlet is much more visible in the SST turbulence model with the variation of the operating point, which could be the trace of a more critical secondary structure developing in that region. The $k-\epsilon$ model, instead, almost does not present at all a variation of eddy viscosity distribution at lower mass-flow.

As a consequence of this behavior, a smaller boundary-layer eddy viscosity and boundary layer dimension for the SST model could therefore possibly reduce the migration of momentum from the mainstream into the boundary layer, decreasing the momentum of the end-wall flow compared to the $k-\epsilon$ model and increasing considerably the cross-flow component. In this way, in the SST model, the end-wall low-momentum flow accumulates on the blade suction side increasing the criticality of possible secondary structures at near-stall conditions. Opposite to this, the larger wall momentum for the $k-\epsilon$ turbulence model would decrease the cross-wise component of the velocity, as already demonstrated with Figure 6.

This difference in the prediction of the eddy viscosity and in the boundary layer height, could be therefore at the origin of the different behavior of the end-wall flow pattern in the rotor hub wall between the two turbulence models.

Moreover, as highlighted in Figure 7, the stagnation point around the leading edge at the hub is the same for the two cases, and therefore the inlet incidence does not play any role in this mechanism.

Anyway, these observation can be considered valid only for the present compressor given the large value of the loading in the hub region. The same conclusions can therefore not be extended to different blade geometries with reduced loading, where the end-wall flow pattern and the evolution of secondary flow structures could assume a less relevant role.

4.3. Impact on large-scale structures

4.3.1. Rotor flow field

The IGV of the present stage was installed to simulate the radial distribution of the flow angle behind a fan and deliver a smooth flow at the rotor inlet, therefore no critical features should take place inside the IGV passage. However, in a highly-loaded rotor blade row, more critical features can appear, such as the tip leakage vortex (TLV) and the hub corner separation, which could lead to flow instabilities and stall inception as mass-flow is reduced [22; 23; 24; 25]. It is therefore worth to detect any possible critical behavior close to the stability limit of the machine looking closer to the casing and hub of the rotor blade.

Figure 9 shows the entropy contour at the rotor casing.

The increased loading at reduced mass-flow induces the streamlines of the tip leakage vortex to become more tangential, with increased entropy gradient across the TLV interface and maximum local entropy. This is visible for both turbulence models. Moreover, at the location of the rotor trailing edge an increase of entropy is representative of a recirculating structure for both turbulence models. However, no clear critical behavior is detected at reduced mass-flow and the flow pattern predicted by the SST and $k-\epsilon$ turbulence models is quite similar for all of the operating conditions.

Figure 10 shows the skin friction lines on the suction side of the rotor blade.

Two flow mechanisms are visible from this picture: a corner separation close to the hub wall and a shock-boundary layer interaction (SBLI) separation in the front part of the blade. The predicted hub corner separation is different for the two models, and the SST

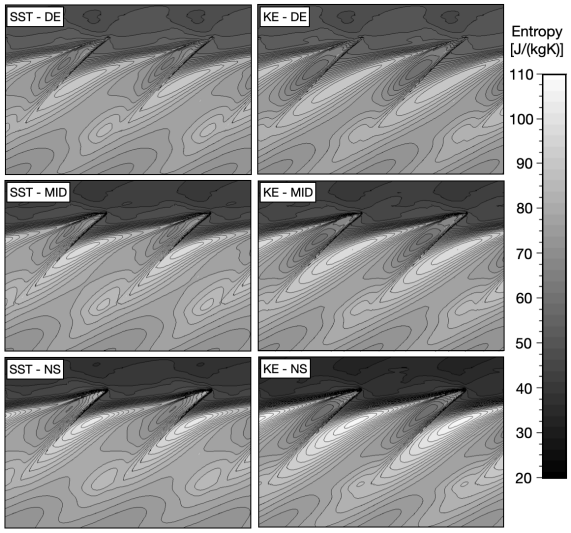

Figure 9: Entropy distribution at casing for SST and $k-\epsilon$ models at DE, MID AND NS conditions.

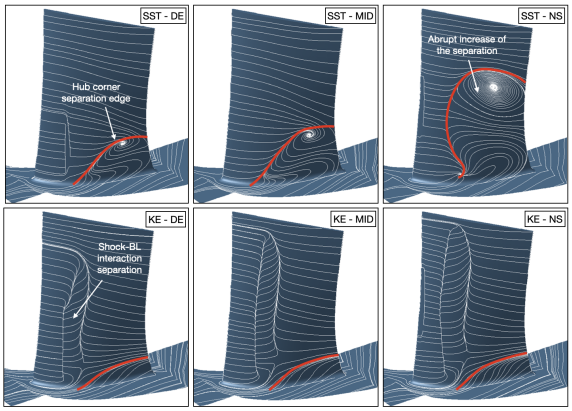

Figure 10: Skin friction lines on rotor blade suction side for SST and $k-\epsilon$ models at DE, MID AND NS conditions.

clearly predicts a larger increase of the corner separation, while for the $k-\epsilon$ this increase is much smoother going form DE to NS. The separation takes place only on the suction side of the blade and on the hub wall the boundary layer keeps attached. The same can be observed in 11, which shows the non-dimensional total pressure map at rotor outlet at near-stall conditions. Concerning the SBLI, only the $k-\epsilon$ model predicts its span-wise and stream-wise variation over the entire operating range of the machine and it assumes larger dimensions with respect to the SST turbulence model. This is a consequence of the reduced eddy viscosity into the main channel for the $k-\epsilon$ model, which reduces the resistance of the boundary-layer to the separation.

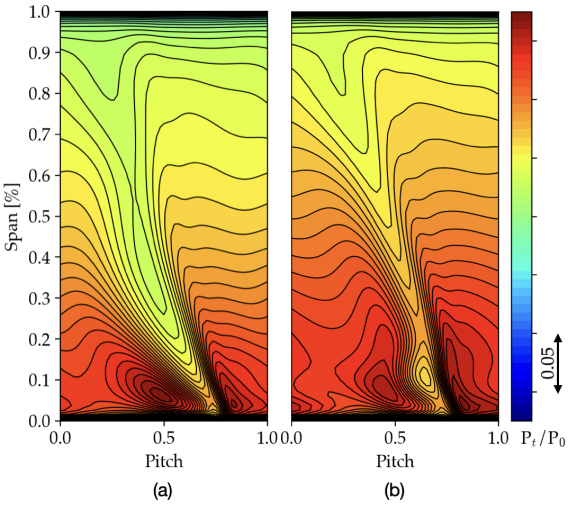

Figure 11: Total pressure map at rotor outlet for SST (a) and $k-\epsilon$ (b) models at near-stall conditions.

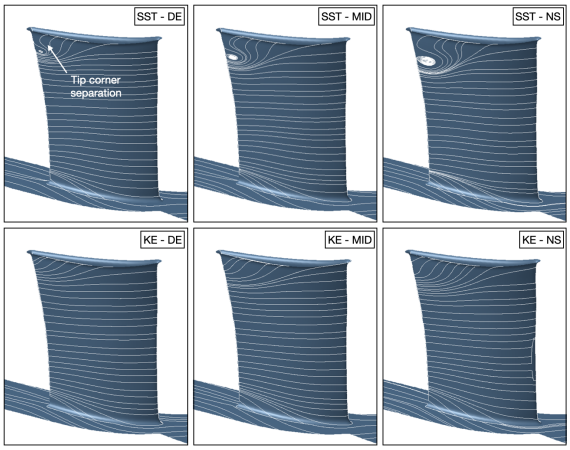

Figure 12: Skin friciton lines on the outlet stator suction side.

It is evident that the reasons behind the different turbulent activity at the rotor outlet are the consequence of a critical development of the rotor hub corner separation for the SST turbulence model. This structure not only reduces the total pressure close to the rotor hub as it happens for the $k-\epsilon$ turbulence model, but involve the entire blade span strongly impacting the losses of the machine (Figure 10). The large loading coefficient of the rotor blade in the hub region (up to 0.75) and the high degree of reaction of the machine (0.86 computed via enthalpy ratios) support this interpretation and the fact that the rotor is prone to develop critical flow structures.

4.3.2. Outlet stator flow field

To check the impact of this structure on the entire flow path of the compressor, the flow pattern on the suction side of the outlet stator is reported in Figure 12.

In the tip region, a corner separation develops but it does not assume the critical behavior of the rotor hub corner one, and it keeps stable all over the operating range of the machine. As expected, the size of the separation increases as mass-flow reduces.

4.3.3. Global performance

It is important to assess the impact of the the detected flow structures on the global performance of the machine. The compressor map non-dimensionalized with respect to the experimental values at design condition, and retrieved with the proposed turbulence models, is shown in Figure 13. The uncertainties linked to the pressure ratio and the mass-flow are reported in the picture (even if the pressure ratio uncertainty is rather small to be visible). The MID operating point is at half operative range with respect to design and near-stall conditions and it is the only point for which an experimental validation does not exist.

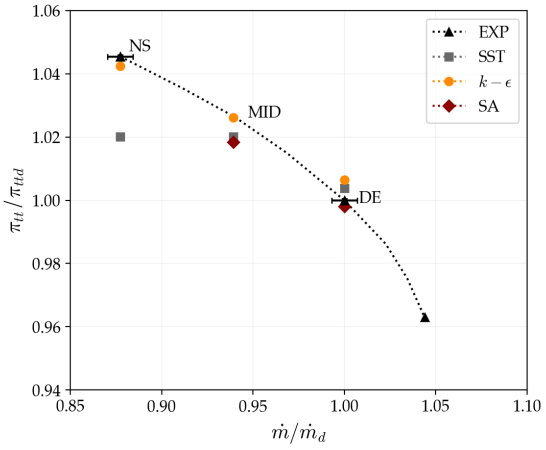

Figure 13: Compressor map obtained by experiments (black) $k-\omega$ SST (grey), $k-\epsilon$ (orange) and SA (red) turbulence models.

At the DE point a difference of 0.62%, 0.38% and 0.2% exists for the pressure ratio predicted by $k-\epsilon$, SST and SA models respectively and the one of the experiments. However, at NS the SST model predicts a totally wrong pressure ratio, as a consequence of the abrupt development of the hub corner separation at reduced mass-flow. The SA model is instead not able to reach the near-stall conditions due to a too strong decrease of the pressure ratio which induces

the simulation to diverge, and only the results at DE and MID operating points are available. This is the reason why only the SST and $k-\epsilon$ turbulence models have been analysed in the paper, as they provide the necessary information to describe possible and different developments of the flow field at NS conditions.

The outcome of this section is that despite the turbulence model impacts on the evolution of the endwall flow pattern and the inlet turbulent quantities all over the operating range of the compressor, at DE condition the overall performance of the compressor is well predicted by both models. However, at reduced mass-flow the turbulence model plays a crucial role as it has a huge impact on the predicted size intensity of the critical flow features, that in this specific case are mainly represented by the hub corner separation.

5. Validation against the experimental results

The reliability of the turbulence model to predict properly flow field and global performance for a specific operating condition is here assessed against the experimental results. As mentioned earlier, only experimental results at design and near-stall operating points are available.

5.1. Span-wise validation at rotor and stator outlets

The comparison of total pressure, temperature and absolute flow angle distributions of the proposed turbulence models against the experimental results is plotted in Figure 14, Figure 15 and Figure 16 in plane 3 (outlet rotor) and plane 4 (outlet of the stage). In these planes, the most important features of the compressor can be observed. The uncertainty for the worst case scenario is reported in the plots.

For the total pressure distributions at rotor outlet, both turbulence models provide results well in agreement with experiments at design conditions, with larger differences in the hub region due to the presence of the corner separation. However at near-stall conditions the results of the $k-\epsilon$ model are better than those of the SST, as expected from the analysis of the compressor map. The TLV evolution, along with the corner separation in the tip region of the stator, determine the differences between experiments and simulations for span location above 60%.

Similar conclusions can be drawn for the total temperature, despite it should be remembered that adiabatic boundary conditions were employed on the solid walls. Indeed, at near-stall conditions the SST model

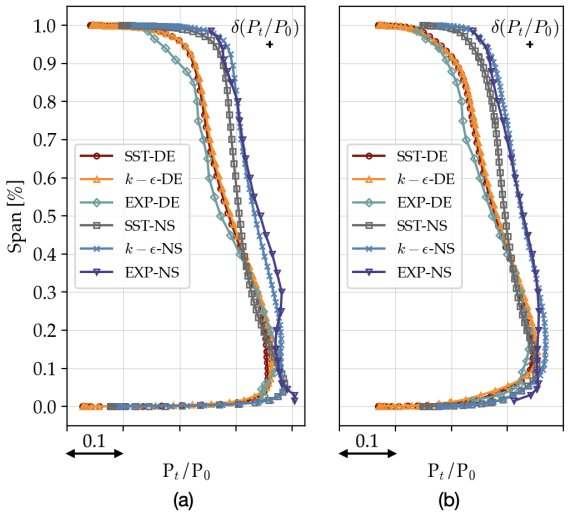

Figure 14: Total pressure predicted by SST and $k-\epsilon$ turbulence models against the experimental results at rotor outlet (a) and stage outlet (b).

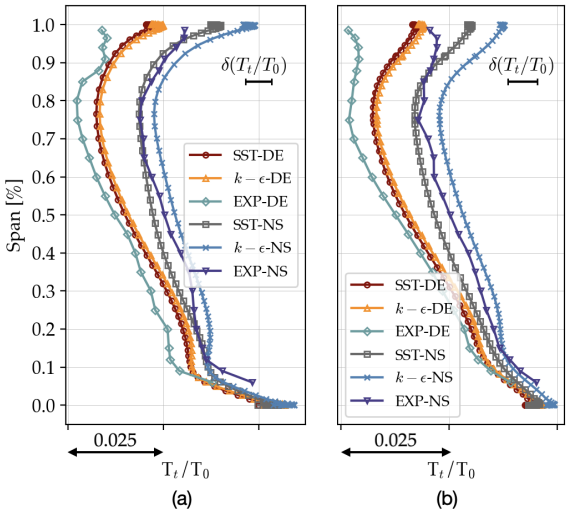

Figure 15: Total temperature predicted by the SST and $k-\epsilon$ turbulence models against the experimental results at rotor outlet (a) and stage outlet (b).

presents better results in the tip region, while the opposite happens on the hub. Both models, at design condition, provide good quality results against the experiments.

For the absolute flow angle at the rotor outlet, the SST model is closer to experiments at near-stall conditions but this depends mainly to the fact that the simulations globally overestimates the flow angle. This is visible also at the stage outlet, where globally the experimental flow angle is 2° smaller than the numerical

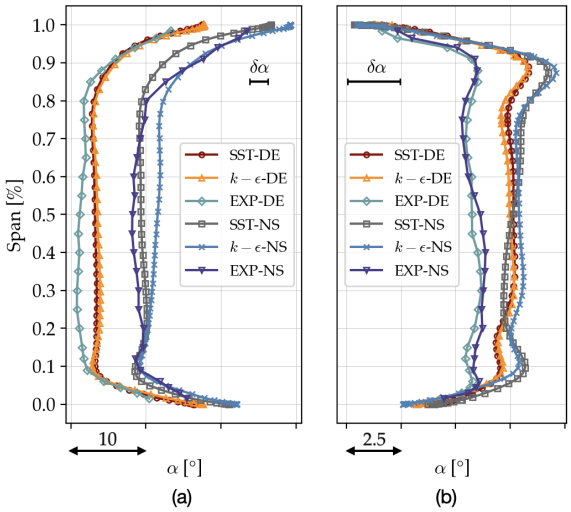

Figure 16: Absolute flow angle predicted by SST and $k-\epsilon$ turbulence models against the experimental results at rotor outlet (a) and stage outlet (b).

one. The reduced $k-\epsilon$ flow angle in plane 3 at 10% span comes from the more axial flow at rotor outlet, as a consequence of the larger end-wall momentum flow, as explained in the previous paragraphs. Moreover, the variation of the operating point impacts largely the flow angle at rotor outlet by an increment of 8° of the flow angle, but the same does not happen at stator outlet, with an angle which keeps constant around 5°.

5.2. 2D validation at rotor outlet

Figures 17 and 18 show a percentage difference of the total pressure at rotor outlet at design and near-stall conditions respectively.

At design conditions (Figure 17), the SST model is more in agreement with the experiments for span lower than 30%. In this region, the maximum percentage difference for the SST model is 3.9%, while for the $k-\epsilon$ model is 5.6%. Close to the tip, instead, they provide similar prediction of the total pressure. At near-stall conditions (Figure 18), the prediction of the two turbulence models is quite similar closer to the hub with a 6.2% difference with respect to experiments, and the SST works properly close to the tip region. However, it completely fails in the prediction of the total pressure at mid-span which is a consequence of the critical development of the separation on the rotor suction side.

6. Conclusions

In the present paper, 3D RANS simulations with the mostly employed turbulence models for the design and analysis of axial compressors were presented, with the intent to assess their influence on the development of the critical flow structures of a highly-loaded compressor. Menter $k-\omega$ SST, Chien $k-\epsilon$, and Spalart Allmaras models were compared, despite for the SA no results were available at NS conditions.

The following conclusions can be drawn from the present analysis:

1. The SST turbulence model develops larger hub cross-flow, which pushes more low-momentum flow toward the suction side of the adjacent blade, enhancing the development of critical flow structures in that region. The opposite behavior is instead visible for the $k-\epsilon$ model. The larger end-wall momentum, indeed, does not allow the horseshoe vortex to impact the rear part of the blade and to accumulate low-momentum flow on the blade corner;
2. The reasons behind such behavior seem to come from the eddy viscosity distribution at the rotor inlet. The lower turbulent viscosity for the SST model in the boundary-layer allows a smaller migration of momentum from the main-flow into the boundary layer with respect to the $k-\epsilon$. This enhances the evolution of tangential cross-flow and critical flow structures on the rotor hub corner.
3. The most critical feature at reduced mass-flow is the separation developing between the rotor suction side and the hub wall. The $k-\epsilon$ turbulence model provides good matching with the experimental global performance, while the SST totally fails this prediction due to the overestimation of the size and intensity of the hub corner separation.
4. The validation against the experimental results shows that no single turbulence model is in general better than the other, and their effectiveness depends on the operating point. At design conditions, the SST model provides better results close to the hub region, while at near-stall operating point it is the $k-\epsilon$ to provide more accurate results. Close to the tip, both models provide results well in agreement with the experiments.

As general outcome, this paper wanted to highlight the effectiveness and weakness of different turbulence models in compressors where the presence of large

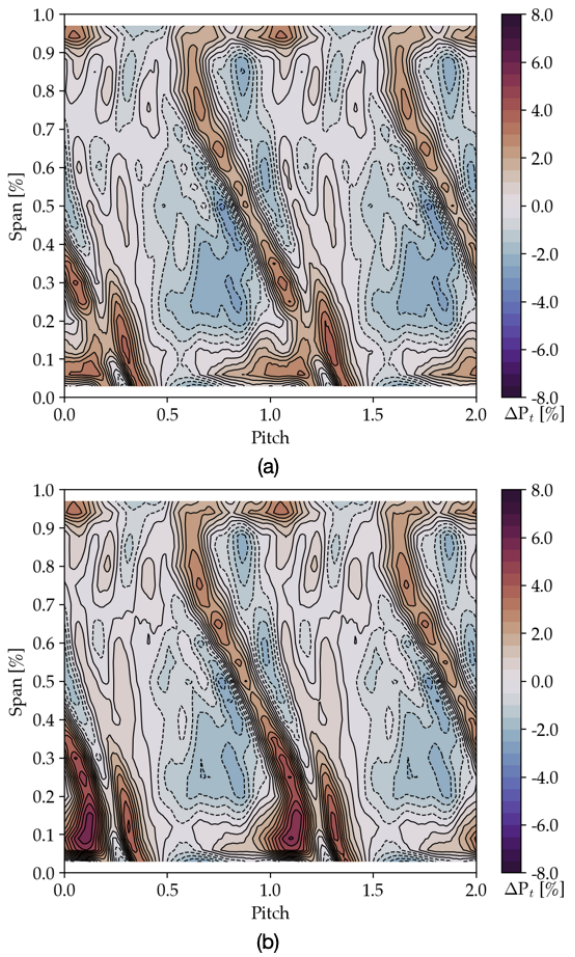

Figure 17: Total pressure percentage difference between SST (a) and $k-\epsilon$ (b) turbulence models against experiments at rotor outlet - DE conditions.

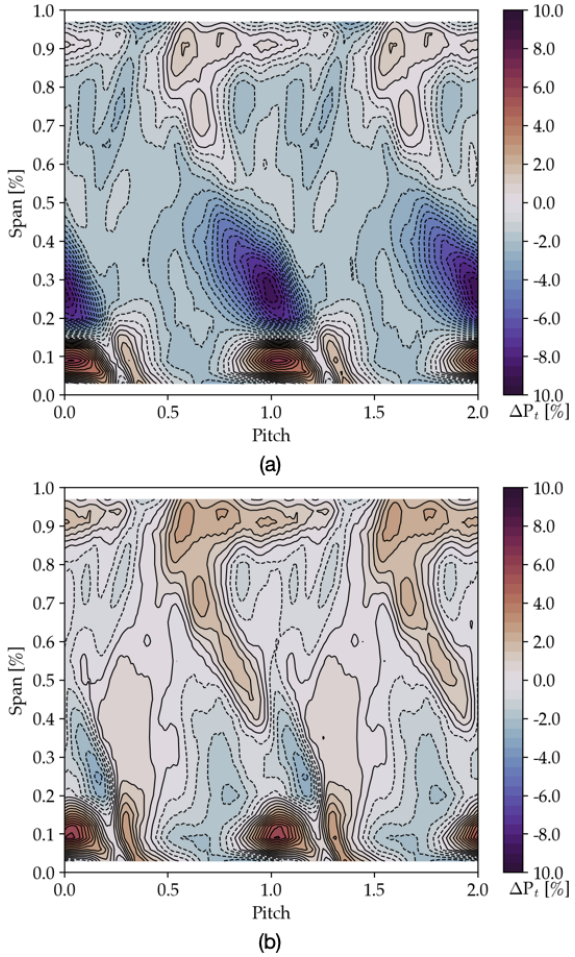

Figure 18: Total pressure percentage difference SST (a) and $k-\epsilon$ (b) turbulence models against experiments at rotor outlet - NS conditions.

scale structures can massively influence the results of a simulation. By doing so, the authors hope to increase awareness about the inherent dangers of relying too much on the results of a single turbulence model to draw conclusions about the evolution of critical flow features and the near-stall behavior of compressors.

Acknowledgments

The authors would like to acknowledge the F.R.S-FNRS for funding the scholarship of Mr. Riccardo Toracchio.

References

[1] Y. Dong, S. J. Gallimore, H. P. Hodson, Three-dimensional flows and loss reduction in axial compressors, Journal of Turbomachinery 109 (3) (1987) 354–361.

[2] J. D. Denton, Loss mechanisms in turbomachines, ASME 93-GT-435 (1993) 1–40.

[3] S. A. Gbadebo, N. A. Cumpsty, T. P. Hynes, Three-dimensional separations in axial compressors, Journal of Turbomachinery 127 (2) (2005) 331–339.

[4] J. D. Denton, W. N. Dawes, Computational fluid dynamics for turbomachinery design, Proceedings of the Institution of Mechanical Engineers, Part C: Journal of Mechanical Engineering Science 213 (2) (1998) 107–124.

[5] R. N. Pinto, A. Afzal, L. V. D'Souza, Z. Ansari, A. D. M. Samee, Computational fluid dynamics in turbomachinery: a review of state of the art, Archives of Computational Methods in Engineering 24 (3) (2017) 467–479.

[6] P. G. Tucker, Trends in turbomachinery turbulence treatments, Progress in Aerospace Sciences 63 (2013) 1–32.

[7] J. Tyacke, N. R. Vadlamani, W. Trojak, , R. Watson, Y. Ma, P. G. Tucker, Turbomachinery simulation challenges and the future, Progress in Aerospace Sciences 110 (2019) 100554.

[8] J. E. Bardina, P. G. Huang, T. J. Coakley, Turbulence modeling validation, testing and development, NASA Technical Memorandum 110446 (1997) 147.

[9] M. R. Simoes, B. J. Montojos, N. R. Moura, J. Su, Validation of turbulence models for simulation of axial flow compressor, in: Proceedings of COBEM, 20th International Congress of Mechanical Engineering, Gramado, RS, Brazil, 2009.

[10] T. Arima, T. Sonoda, M. Shirotori, A. Tamura, K. Kikuchi, A numerical investigation of transonic axial compressor rotor flow using a low-Reynolds-number $k - \epsilon$ turbulence model, Journal of Turbomachinery 121 (1) (1999) 44–58.

[11] F. Ning, L. Xu, Numerical investigation of transonic compressor rotor flow using an implicit 3D flow solver with one-equation Spalart-Allmaras turbulence model, in: Proceeding of ASME Turbo Expo, New Orleans, Louisiana, USA, 2001, 2001-GT-0359.

[12] Y. Song, J. Donghai, D. Xingmin, Z. Fangs, Application and comparison of SST model in numerical simulation of the axial compressors, Journal of Thermal Science 19 (4) (2010) 300–309.

[13] X. He, F. Zhao, M. Vahdati, Evaluation of Spalart-Allmaras turbulence model forms for a transonic axial compressor, in: Proceedings of Global Power and Propulsion Society, GPPS Chania, 2020, gPPS-CH-2020-0013.

[14] M. V. Casey, Validation of turbulence models for turbomachinery flows - a review, Engineering Turbulence Modelling and Experiments *V*, Elsevier Science Ltd (2002) 43–57.

[15] Y. Liu, X. Yiu, B. Liu, Turbulence models assessment for large-scale tip vortices in an axial compressor rotor, Journal of Propulsion and Power 24 (1) (2008) 15–25.

[16] H. Zhang, Y. Wu, Y. Li, Evaluation of RANS turbulence models in simulating the corner separation of a high-speed compressor cascade, Engineering Applications of Computational Fluid Mechanics 9 (1) (2015) 477–489.

[17] L. Yangwe, Y. Hao, L. Yingjie, L. Lipeng, L. Qiushi, Numerical study of corner separation in a linear compressor cascade using various turbulence models, Chinese Journal of Aeronautics 29 (3) (2016) 639–652.

[18] H. Yan, Y. Liu, Q. Li, L. Lu, Turbulence characteristics in corner separation in a highly loaded linear compressor cascade, Aerospace Science and Technology - AESCTE 4378 75 (2018) 139–154.

[19] ANSI, ASME, ANSI/ASME PTC 19.1-2005 measurement uncertainty, American Society of Mechanical Engineers.

[20] G. Dell'Era, N. Habotte, J. Desset, J.-F. Brouckaert, S. Hiernaux., Experimental characterization of stall phenomena in a single-stage low-pressure axial compressor, Journal of Power and Energy 229 (5) (2015) 549–559.

[21] Numeca International, Fine/Turbo theory guide, 13th Edition (2019).

[22] C. Hah, J. Loellbach, Development of hub corner stall and its influence on the performance of axial compressor blade rows, Journal of Turbomachinery 121 (1) (1999) 67–77.

[23] M. Choi, J. H. Baek, S. H. Oh, D. J. Ki, Role of the hub-corner-separation on the rotating stall, 42nd AIAA/ASME/SAE/ASEE Join Propulsion Conference Exhibit - AIAA 2006 (2006) 4462.

[24] S. A. Weichert, Tip clearance flows in axial compressors: stall inception and stability enhancement, PhD Thesis, University of Cambridge, Department of Engineering, Cambridge, MA (September 2011).

[25] M. H. Smith, G. Pullan, S. D. Grimshaw, E. M. Greitzer, Z. S. Spakovszky, The role of tip leakage flow in spyke-type rotating stall inception, in: Proceedings of ASME Turbo Expo, Charlotte, NC, USA, 2017, gT2017-63655.